



**This is a self-archived version of an original article. This version may differ from the original in pagination and typographic details.**

**Author(s):** Harjupatana, Tero; Miettinen, Arttu; Kataja, Markku

**Title:** A method for measuring wetting and swelling of bentonite using X-ray imaging

**Year:** 2022

**Version:** Published version

**Copyright:** © 2022 The Author(s). Published by Elsevier B.V.

**Rights:** CC BY 4.0

**Rights url:** <https://creativecommons.org/licenses/by/4.0/>

**Please cite the original version:**

Harjupatana, T., Miettinen, A., & Kataja, M. (2022). A method for measuring wetting and swelling of bentonite using X-ray imaging. *Applied Clay Science*, 221, Article 106485.  
<https://doi.org/10.1016/j.clay.2022.106485>



## A method for measuring wetting and swelling of bentonite using X-ray imaging

Tero Harjupatana\*, Arttu Miettinen, Markku Kataja

*Department of Physics, University of Jyväskylä, P.O. Box 35 (YFL), FI-40014, Finland*



### ARTICLE INFO

**Keywords:**  
X-ray imaging  
Water content  
Water transport  
Deformation  
Bentonite  
Swelling

### ABSTRACT

A non-invasive method based on X-ray imaging for measuring deformation and water transport in wetting and swelling bentonite samples is introduced. Sequential X-ray images taken of the samples were used to calculate the attenuation coefficient and deformation. These results, together with careful calibration, allowed finding the dry density and water content distributions and their temporal evolution in the wetting and swelling samples. A specific correction technique, based on regularly taking reference X-ray images of aluminum plates of varying thickness, was developed and used to take into account X-ray beam instabilities and thus to improve the accuracy of density analysis. Large deformation, present in the experiments, was measured with an improved version of a block-matching algorithm. The X-ray imaging method was used here to measure the axial swelling of compacted MX-80 bentonite samples in a tube when in contact with saline solution (0.1 M NaCl). This setup mimics a scenario where bentonite, planned to be used as a buffer material in a nuclear waste repository placed deep in the bedrock, swells into a rock fracture filled by groundwater. The method yielded potentially valuable data on hydro-mechanical behavior of bentonite, which may be used in developing and validating material models to be used in safety assessment of nuclear waste repository concepts.

### 1. Introduction

Transport of liquids in porous materials is of great interest in many areas, e.g., in biology, soil sciences and construction technology. Non-destructive methods based, e.g., on electromagnetic and neutron radiation, and on nuclear magnetic resonance imaging have been used to monitor liquid transport in related applications (Zhou et al., 2014; Jung et al., 2012; Shafizadeh et al., 2015; Terskikh et al., 2005). Most methods are, however, restricted to cases where the deformation of the solid matrix can be neglected. Yet, many materials swell or shrink notably with variations of liquid content. Simultaneous monitoring of both solid and liquid content would therefore be useful, e.g., in developing and validating hydro-mechanical material models. To this end, the authors previously introduced a method based on X-ray tomography for measuring deformation and water transport in bentonite samples wetted in a constant volume (Harjupatana et al., 2015). The technique was later successfully applied to measure wetting and swelling of a wood-fibre reinforced composite material (polylactic acid and birch pulp) (Miettinen et al., 2016). In both studies, a simple block-matching algorithm was adequate to measure small deformation. The water

transport and deformation were also relatively slow (experiment duration 1–20 weeks) compared to the scan duration (1–4 h), and thus the time resolution was sufficient. X-ray tube based microtomography devices, as used here, produce high-resolution 3D images but have quite long scan times (typically from several minutes to tens of hours) depending on sample type, sample size and desired image quality. Those devices are thus suitable to monitor relatively slow processes only.

Bentonite is a clay material with high montmorillonite content, and it swells strongly in the presence of water. Due to its swelling ability and low permeability for water, a bentonite layer is often used as a groundwater seal on various waste sites and ponds (Koch, 2002). Bentonite is also suggested to be used as a buffer material between the waste canisters and the bedrock in nuclear waste disposal concepts in many countries, e.g., in Finland (Juvankoski, 2013), Sweden (Börjesson et al., 2010) and Switzerland (Nagra, 2009). There, a particular risk is the possible erosion of bentonite through groundwater filled macroscopic fractures in the bedrock, which may expose the waste canisters to groundwater (Neretnieks et al., 2009; Reid et al., 2015).

The main goal of this work was to develop a method applicable for producing experimental data to support modeling the behavior of the

\* Corresponding author.

E-mail address: [tero.t.harjupatana@jyu.fi](mailto:tero.t.harjupatana@jyu.fi) (T. Harjupatana).

**Table 1**

Result of sieve analysis for MX-80 bentonite. The mean and standard deviation (SD) were calculated from three repetitions.

Sieve size [mm]	Mass passed [%] (mean $\pm$ SD)
2.000	99.9 $\pm$ 0.1
1.000	98.9 $\pm$ 0.2
0.500	66.5 $\pm$ 1.5
0.250	34.4 $\pm$ 1.6
0.125	16.0 $\pm$ 1.0
0.100	11.9 $\pm$ 0.8
0.050	3.2 $\pm$ 0.2

**Table 2**

Mineralogical properties for MX-80 bentonite ([Karnland et al., 2006](#); [Karnland, 2010](#)).

Mineral composition (Wt%)	Montmorillonite (81.4%), Tridymite (3.8%), Plagioclase (3.5%), Muscovite (3.4%), Quartz (3.0%), Cristobalite (0.9%), Gypsum (0.9%), Illite (0.8%), Pyrite (0.6%), Lepidocrocite (0.5%), Hematite (0.4%), Anatase (0.2%), Calcite (0.2%), Magnetite (0.2%), Goethite (0.1%), Microcline (0.1%)
Cation exchange capacity	0.75 eq/kg
Exchangeable cations	Na <sup>+</sup> (0.55 eq/kg), Ca <sup>2+</sup> (0.13 eq/kg), Mg <sup>2+</sup> (0.05 eq/kg), K <sup>+</sup> (0.01 eq/kg)
Structural formula for montmorillonite	Na <sub>0.46</sub> Ca <sub>0.05</sub> Mg <sub>0.02</sub> K <sub>0.01</sub> (Si <sub>7.94</sub> Al <sub>0.06</sub> ) <sub>4</sub> Fe <sub>0.37</sub> <sup>3+</sup> Mg <sub>0.50</sub> O <sub>20</sub> (OH) <sub>4</sub>
Grain density	2.75–2.78 g/cm <sup>3</sup>

bentonite buffer in a scenario where erosion might take place. To reproduce the wetting and swelling of the bentonite buffer emplaced in a repository tunnel, the actual fracture in a rock was simulated by a simplified tube geometry. Part of the vertical sample holder tube was filled with compacted bentonite and exposed to saline solution, leading to approximately one-dimensional axial transport of water and swelling of bentonite. Instead of X-ray tomography, the resulting fast swelling was monitored using X-ray imaging, which allows to study much faster processes, but is limited to simpler sample geometries. A substantial improvement, a correction technique that takes into account angular and temporal instabilities of the X-ray beam was developed and used to increase the accuracy of density analysis. Furthermore, the block-

matching algorithm used to find the displacement field of the solid material was improved to account for large deformations. The X-ray imaging method was applied here to 16 bentonite swelling experiments, where the initial dry density and the initial water content of the samples were varied.

## 2. Materials

The sample material was Wyoming type bentonite under the brand name MX-80. The grain size distribution of this granular material was measured using a sieve analysis ([Table 1](#)). The largest particles were around 1 mm in diameter while the mass average diameter of grains was around 0.4 mm. Mineralogical properties of MX-80 bentonite are given in [Table 2](#). MX-80 has a high montmorillonite content (81%), while silica minerals quartz and its polymorphs tridymite and cristobalite make up 8% of the total mass, and the rest consist of different accessory minerals. The cation exchange capacity values and the structural formula for montmorillonite show that sodium is the dominant cation. Wyoming bentonites, such as MX-80, are known as high-grade sodium bentonites having high swelling capacity.

Bentonite powder and samples were wetted with saline solution (0.1 M NaCl), which approximated the sodium concentration (0.115 M Na<sup>+</sup>, dominant cation) in the current groundwater at the depth (465 m) of nuclear waste repository at Olkiluoto, Finland ([Hellä et al., 2014](#)), but neglected other cations and components (in particular 0.033 M Ca<sup>2+</sup>).

## 3. Experimental setup and procedure

### 3.1. Sample holder and samples

The sample holder consisted of a vertical aluminum tube of inner diameter 10 mm, wall thickness 1 mm, and height 95 mm, attached to a mounting plate ([Fig. 1](#)). A proper amount of preconditioned (see below) MX-80 bentonite powder was placed in the sample holder tube and compacted to form a sample of height 20 mm. The bottom end of the sample was firmly against a porous sintered glass filter disc (pore diameter 10–16  $\mu\text{m}$ ), which allowed pore air to be released from the sample. Compacting the samples directly into the tube eliminated gaps between the sample and the tube, which could have acted as water

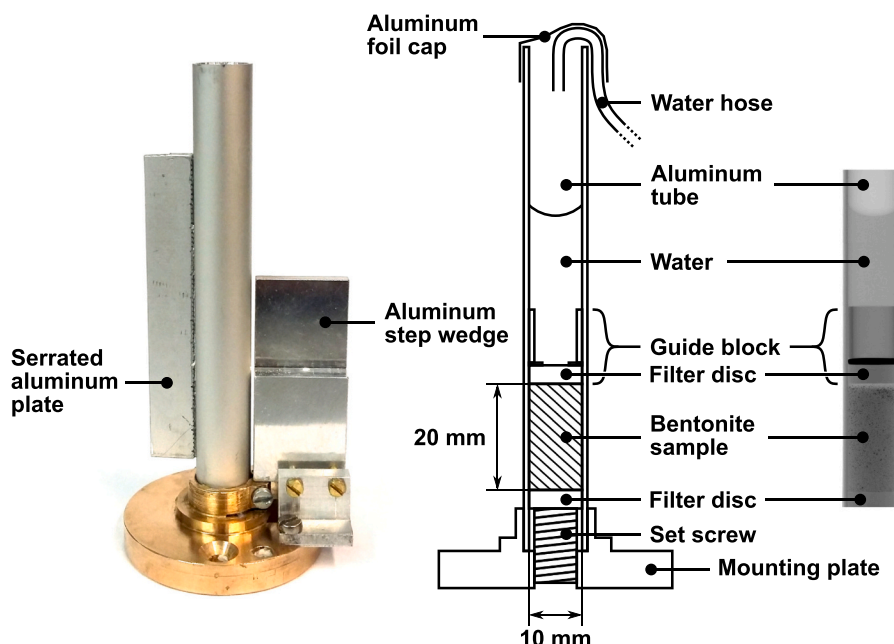


**Fig. 1.** Photo (left), schematic cross-sectional view (middle) and X-ray image (right) of sample holder.

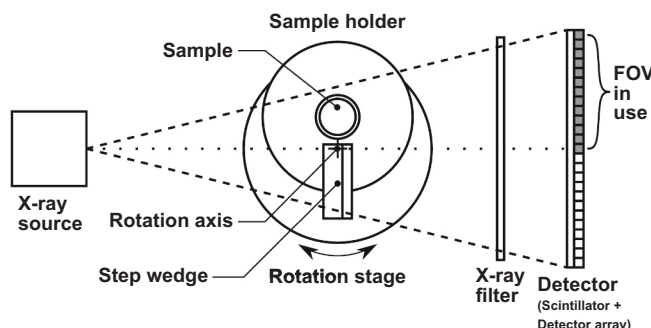


**Fig. 2.** Schematic top view of X-ray imaging setup (not to scale). The generated X-rays traversed through a sample and were detected with a scintillator plate and a detector array. An X-ray filter (exceptionally located on the detector side here) was used to cut the lower part of the energy spectrum. The sample holder was attached non-concentrically on the rotation stage, and a half of the FOV was in use (shaded pixel columns). This allowed to take the necessary reference images by rotating the stage by 180°.

transport channels. A freely-moving guide block ( $m = 1.5$  g), consisting of a porous filter disc (similar to the bottom one), a steel washer and a short piece of aluminum tube, was placed on the top of the sample. The guide block ensured that the top surface of the sample remained flat and well defined during the swelling process. An aluminum step wedge with 3 mm and 8 mm thick steps, and a serrated aluminum plate were installed alongside the tube to facilitate beam hardening correction and image stitching procedures, respectively (see sections 4.1 and 4.2).

Eight different combinations of initial dry density values 1.40 g/cm<sup>3</sup>, 1.65 g/cm<sup>3</sup> and 1.80 g/cm<sup>3</sup> and water content values 12%, 17% and 24% were examined with two repetitions for each possible case (1.80 g/cm<sup>3</sup> and 24% is unfeasible, see Eq. 19). Here, the water content is defined as  $w = m_w/m_b = \rho_w/\rho_b$ , where  $m_w$  and  $m_b$  are the masses of water and bentonite in volume  $V$ , and  $\rho_w = m_w/V$  and  $\rho_b = m_b/V$  are the partial densities of water and bentonite. The partial density of bentonite is also called 'dry density'. The initial water content of the powder was about 12% in storage conditions, measured by oven drying at 105 °C. The two higher initial water content values were achieved by spraying the bentonite powder with saline solution (0.1 M NaCl) and mixing thoroughly. A small amount of iron particles of diameter around 100 µm (1.5% by weight) were mixed with the powder to act as tracer particles in the X-ray images so that deformation could be measured. This particle density and size was tested to be suitable in this work.

### 3.2. X-ray imaging

In X-ray imaging, the sample is illuminated with X-rays, and the partially attenuated intensity is measured by a detector array (Fig. 2). Typically, the detector has a scintillator plate, which converts X-rays into visible light. This light is then converted into a digital X-ray image by using an image sensor array coupled to suitable optics. Ideally, the grayscale values of an X-ray image are proportional to the intensity of the X-ray beam incident to the scintillator. The attenuation of a narrow monochromatic X-ray beam is described by the Beer-Lambert law

$$\frac{I}{I_0} = \exp \left[ - \int_c^x \mu(x) dx \right], \quad (1)$$

where  $I$  is the attenuated intensity,  $I_0$  is the unattenuated intensity,  $I/I_0$  is the transmittance,  $\mu$  is the linear attenuation coefficient and  $x$  is the position along the line ( $C$ ) from the source to the detector. From here on, the quantities  $I$  and  $I_0$  are directly used to denote X-ray images;  $I$  is the dark-field corrected X-ray image and  $I_0$  is the dark-field corrected background image (i.e., the X-ray image taken without a sample). The

**Table 3**  
Five-stage X-ray image acquisition process.

Stage	Number of images	Time interval between images	Total time	Description
0	1	–	–	Initial state, unwetted sample
1	29	20 s	10 min	Fast initial swelling
2	30	4 min	2 h	Transitional swelling
3	279	20 min	95 h	Slow late stage swelling
4	1	–	–	Final state, frozen sample

dark-field correction is a simple subtraction  $I = I' - I_D$ , where  $I'$  is the uncorrected X-ray image and  $I_D$  is the dark image (i.e., the image taken without X-rays).

For compounds and mixtures, the linear attenuation coefficient is given by the mixture rule

$$\mu = \sum_i c_i \rho_i, \quad (2)$$

where  $c_i = (\mu/\rho)_i$  and  $\rho_i$  are the mass attenuation coefficient and the partial density of each constituent, respectively (Hubbell and Seltzer, 1995). The mass attenuation coefficient depends on the elemental composition of the material and on the X-ray energy, but is expected to be independent of density.

The X-ray imaging was performed using a SkyScan 1172 microtomography scanner in X-ray imaging mode with 1000 (H) × 524 (V) pixels and 32 µm pixel size. This pixel size was sufficient to capture the 100 µm iron particles, and resulted in the field of view (FOV) 32 (H) mm × 17 (V) mm. As there was no option to move the rotation stage sideways (normal to source-detector line), the sample holder was attached non-concentrically on the rotation stage of the scanner (Fig. 2). This conveniently allowed to take reference X-ray images of the background ( $I_0$ ) and of the two aluminum plates in the step wedge ( $I_{r1}$  and  $I_{r2}$ ) by rotating the stage by 180°. The rotation angle was set to 0° when the sample was imaged and to 180° when the reference images were taken. This procedure halved the usable FOV of a single image to 16 (H) mm × 17 (V) mm. The FOV was, however, extended in the vertical direction to 16 (H) mm × 65 (V) mm by stitching five images taken from different vertical positions with 12 mm spacing. Here, the rotation stage was moved in the vertical direction while the X-ray source and the detector were in fixed positions. The X-ray tube was operated with an acceleration voltage of 100 kV and a current of 80 µA. The low energy part of the X-ray spectrum was attenuated using a built-in filter plate with 0.5 mm aluminum and 0.04 mm copper layers. The exposure time for a single X-ray image was 1106 ms, but the average of 10 images was used to improve the signal-to-noise ratio. The total image acquisition time, including the time needed for the reference images and sample movements, was approximately 4 min for the extended FOV. Each X-ray image taken was automatically dark-field corrected by the scanner. The pixel values of the dark images were very small ( $\langle I_D/I_0 \rangle \approx 0.2\%$ ) and stable during the experiments. A new dark image was taken before each experiment.

### 3.3. Measurement procedure

After sample preparation, the sample holder was attached to the rotation stage of the scanner, and a water hose, pulled into the scanner through a cable lead-in, was put into the sample holder tube (Fig. 1). The open top end of the tube was sealed with aluminum foil to prevent the evaporation of water. The X-ray source was turned on and let to stabilize about 1 h. Thereafter, a five-stage X-ray image acquisition process was started (Table 3). The first X-ray image was taken of the unwetted sample (stage 0). The wetting was then initiated by injecting water into the upper part of the sample holder tube. The wetting and swelling

process was monitored for about four days using three different imaging procedures (stages 1–3), where the time interval between the images was increased at each stage as the swelling slowed down. In stage 1, the fast initial swelling was captured by using the single image FOV at only one vertical position covering the upper end of the sample. Also omitting the reference images reduced the time interval between X-ray images to 20 s in this stage. The X-ray images from the other positions, assumed not to be affected by the wetting, were copied from stage 0 and used to construct the extended FOV image of the entire sample. The reference images for stage 1 were interpolated from those taken in stages 0 and 2. At the end of the experiment, the sample holder was detached and dipped into liquid nitrogen, thereby freezing the sample thoroughly. The sample holder was reattached into the scanner and an X-ray image of the frozen sample was taken (stage 4). The sample holder was again detached and the tube and the sample were cut into 4–6 slices of thickness 6.8 mm (the number of slices depended on the final height of the sample). The freezing ensured that the sample, especially the soft upper part, was solid and thus it could be properly handled and sliced. The masses of bentonite and water in the slices were determined gravimetrically by oven drying at 105 °C at least 14 h. As the dimensions of the slices were also measured, the average partial densities of bentonite and water in the slices could be calculated. These data were used to validate the method and estimate the overall error of the results (see section 5).

#### 4. Image processing and data analysis

##### 4.1. Local beam hardening correction

Beam hardening is an artifact related to the use of a polychromatic X-ray source such as an X-ray tube. When X-rays traverse through a material, the average energy of the beam increases as the lower energy X-ray photons are attenuated more efficiently than the higher energy ones. In this case, the effective linear attenuation coefficient depends on material thickness and the Beer-Lambert law (Eq. 1) is not accurate. Correcting for beam hardening is usually not necessary in conventional X-ray imaging, e.g., when density differences are inspected qualitatively. However, in X-ray tomography the beam hardening correction (BHC) is a standard procedure. A widely used phenomenologically justified method is to use a quadratic correction of the form (Herman, 1979; Hsieh et al., 2000; Zou et al., 2011)

$$\ln\left(\frac{I}{I_0}\right)_c = A_1 \cdot \ln\left(\frac{I}{I_0}\right)_m + A_2 \cdot \ln^2\left(\frac{I}{I_0}\right)_m, \quad (3)$$

where the subscripts c and m denote the corrected and measured transmittances, respectively. Typically, the value of the coefficient  $A_1$  is set to 1, and the operator visually finds a value for the coefficient  $A_2$  such that the effect of the beam hardening (the cupping artifact) appears minimized in the reconstructed images.

The energy spectrum of the conical X-ray beam produced by an X-ray tube may include small spatial and temporal variations caused, e.g., by the anode heel effect (Bushberg et al., 2002) and by instabilities in the X-ray focal spot (Zhou et al., 2016). Some variations may also be caused by the detector. In the standard BHC these small variations are neglected and the same value of coefficient  $A_2$  is used to correct all the pixels in a set of X-ray images that may be acquired over a prolonged time. The present method is sensitive to these variations as it utilizes X-ray images to measure small density differences in swelling and wetting bentonite samples. Thus, a specific correction procedure, called here a local beam hardening correction (LBHC), was developed to simultaneously correct the effect of beam hardening and its variations. A similar method was recently introduced also by Gutschin et al. (2019) to improve image quality in X-ray tomography. The LBHC is based on selecting a suitable homogeneous reference material for which the Beer-Lambert law (Eq. 1) can be written in a form

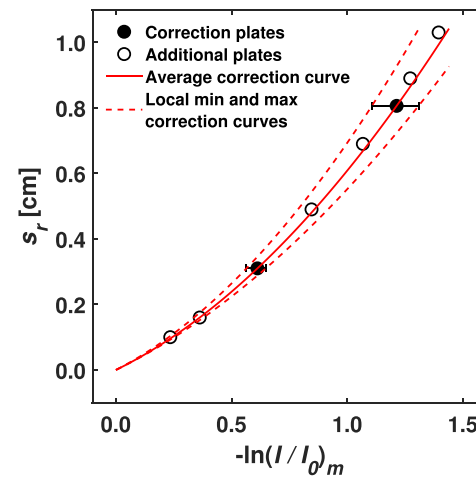


**Fig. 3.** Local beam hardening correction. The solid line is the correction curve (Eq. 5) for the averaged data from the aluminum correction plates in the step wedge (solid circles). The horizontal error bars and the dashed lines illustrate the local variation across the FOV. The open circles show the averaged data from additional aluminum plates used only here to validate the correction method.

$$\ln\left(\frac{I}{I_0}\right)_c = -\mu_r s_r, \quad (4)$$

where  $\mu_r$  is the linear attenuation coefficient and  $s_r$  is the thickness of the reference material. Combining Eq. 3 and 4 yields

$$s_r = A'_1 \cdot \ln\left(\frac{I}{I_0}\right)_m + A'_2 \cdot \ln^2\left(\frac{I}{I_0}\right)_m, \quad (5)$$

where  $A'_i = -A_i/\mu_r$ . This form (Eq. 5) transforms the measured transmittance into the equivalent thickness of the reference material.

The effect of beam hardening is best corrected when the mass attenuation coefficients of the sample and reference materials have similar energy dependence. This is the case for materials having comparable values of effective atomic number  $Z_{\text{eff}}$ , which can be calculated for compounds using the approximate formula (Johns and Cunningham, 1983)

$$Z_{\text{eff}}^{3.5} = \sum_i f_i Z_i^{3.5}, \quad (6)$$

where  $f_i$  and  $Z_i$  are the fraction of electrons and the atomic number of atom  $i$  in the compound, respectively. By using an empirically determined composition of MX-80 bentonite (Table 2) and the chemical formula for water, Eq. 6 gives  $Z_{\text{eff,b}}=12.8$  and  $Z_{\text{eff,w}}=7.5$ . Here, an appropriate reference material was thus found to be aluminum ( $Z_{\text{Al}}=13$ ). With this choice the method can be expected to be sufficiently accurate for bentonite, but may lead to slight overcorrection for pure water.

The coefficients  $A'_i$  were solved locally by forming two simultaneous equations from Eq. 5 using the measured transmittances ( $I_{r1}/I_0$  and  $I_{r2}/I_0$ ) and the thicknesses of the two aluminum correction plates ( $s_{r1} = 3$  mm and  $s_{r2} = 8$  mm) present in the step wedge (see Figs. 1 and 2). The coefficients were first solved for subregions of size  $10 \times 10$  pixels, and then interpolated to individual pixels. This accuracy was found sufficient to resolve the inhomogeneities of the X-ray source and, on the other hand, to provide sufficient averaging to reduce noise. Exemplar data and correction curves are shown in Fig. 3. The correction is in good agreement with the data from additional aluminum plates measured separately, and not used in solving the coefficients  $A'_i$ . The error bars and the minimum and maximum local correction curves show the spatial

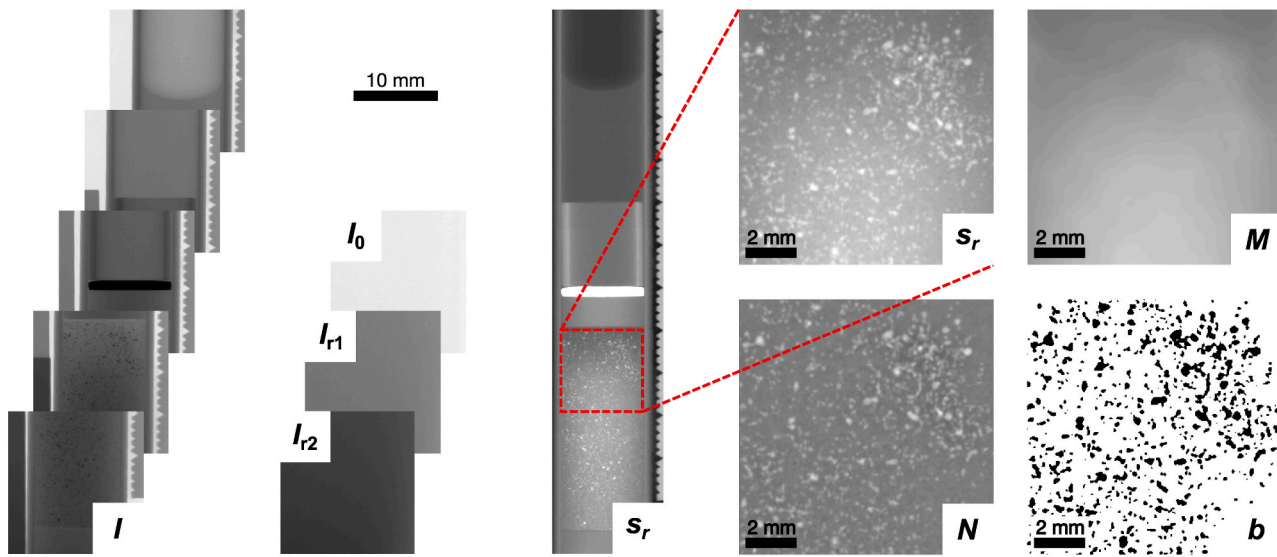


**Fig. 4.** Image processing procedure. The partly overlapping X-ray images ( $I$ ), taken at various vertical positions of the sample holder tube, were first converted to aluminum equivalent thickness images using the reference images ( $I_0$ ,  $I_{r1}$  and  $I_{r2}$ ) and then stitched to form a combined aluminum equivalent thickness image of the sample and the tube ( $s_r$ ). A normalized image ( $N$ ) was formed by subtracting the median filtered image ( $M$ ) from the stitched image ( $s_r$ ). The normalized image was further thresholded to form a binary mask image ( $b$ ). The visibility of the serrated plate in the stitched image ( $s_r$ ) has been enhanced in this figure.

variation of the correction across the FOV.

#### 4.2. Stitching, normalization and thresholding

The image processing procedure is illustrated in Fig. 4. After applying the LBHC to the X-ray images taken ( $I$ ), the FOV was extended by stitching the aluminum equivalent thickness images ( $s_r$ ). This was done by appropriately cropping the images, and joining the cropped images vertically together to achieve a continuous image of the entire sample tube. The serrated aluminum plate was used to visually verify the accuracy of the stitching process. The stitched images were 2D median filtered with a radius large enough so that the tracer particles disappear leaving approximate background visible ( $M = \text{Median}\{s_r\}$ ). Normalized images were then formed by subtracting this background from the stitched images ( $N = s_r - M$ ). The deformation of the samples was measured using the normalized images (see section 4.3). The normalized images were further thresholded to form binary mask images  $b = H(N_{th} - N)$ , where  $H$  is the Heaviside step function and  $N_{th}$  is the threshold value that sets the pixels containing tracer particles to 0 and the other pixels to 1. The binary mask images were used to exclude the tracer particles from the stitched images ( $s_r$ ), which were used to calculate the attenuation coefficient (see section 4.4).

#### 4.3. Deformation

The displacement  $u_z$  at position  $z$  in the sample was calculated using a two-dimensional block-matching algorithm, applied to the normalized images ( $N$ ). As the swelling of bentonite in the present tube geometry was approximately one-dimensional, the displacements were measured only in the axial direction ( $z$ ). A rectangular reference block  $B_{\text{ref}}(z)$ , a subimage of  $m$  (H)  $\times$   $n$  (V) pixels centered at  $z$ , was first extracted from the initial state image. Blocks of similar size  $B(z + u_z)$  were then extracted from the deformed state image at different pixel positions ( $u_z = 0, \pm 1 \text{ px}, \pm 2 \text{ px}, \dots$ ). The minimum of the mean squared difference

$$\text{MSD}(u_z, z) = \frac{1}{mn} \sum_{i=1}^n \sum_{j=1}^m [B_{ij}(z + u_z) - B_{\text{ref},ij}(z)]^2 \quad (7)$$

yielded the displacement  $u_z$  at location  $z$ . Subpixel accuracy was achieved by fitting a quadratic polynomial to the MSD values near its

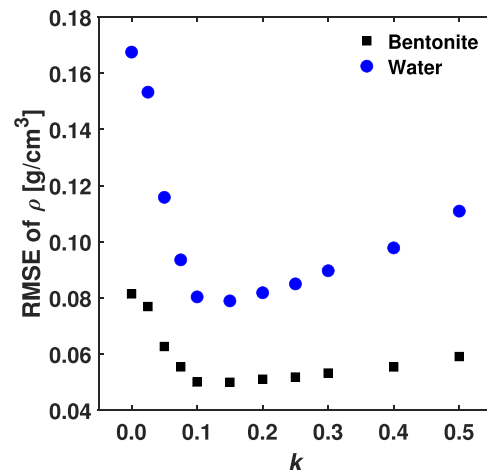


**Fig. 5.** Root-mean-square error (RMSE) of partial densities of bentonite and water between results and validation data as a function of block update parameter  $k$  (Eq. 9). Each point of the graph represents the RMSE value of 160 data points (16 samples  $\times$  10 layers).

minimum, and using the location of the minimum of the polynomial as the final value of displacement.

In general, such a block-matching algorithm leads to satisfactory results in cases where no significant local deformation of the material between the compared blocks takes place, i.e., the displacement corresponds to pure translation. However, here the bentonite swelled locally many times of its original volume and resulted in low correlation between the blocks extracted from the initial state image and from the images taken some time later. This, in turn, led to reduced accuracy in finding the value of displacement corresponding to the minimum of  $\text{MSD}(u_z, z)$ . Updating the entire reference image to the current image after each time step did not help to avoid such a problem, but resulted in significant cumulative error of displacement at later times. To minimize the total error, an optimized method was used such that the reference block was locally updated only whenever the correlation between the block from the current deformed state image and the reference block

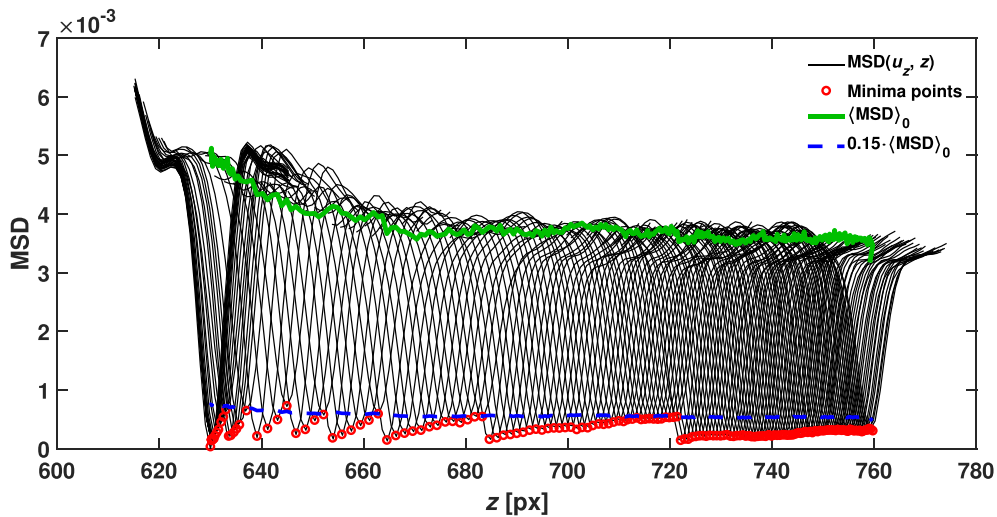


**Fig. 6.** Calculation of displacement at a grid point. The minima points of the MSD curves gave the new positions of the material initially at the grid point ( $z = 630$  px). The minimum value of the MSD increased with decreasing correlation as the bentonite deformed. The reference block was repeatedly updated according to the criterion given by Eq. 9 leading to sudden decrease of the minimum value at corresponding locations. Here, only every second MSD curve is shown for clarity.

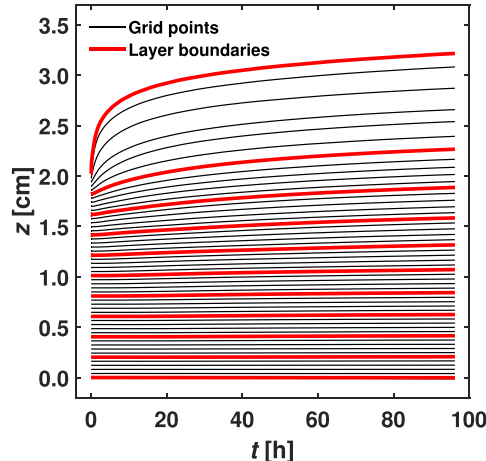


**Fig. 7.** Measured deformation for sample 5B ( $\rho_{b0} \approx 1.65 \text{ g/cm}^3$ ,  $w_0 \approx 17\%$ , see section 5). The positions of the grid points and the layer boundaries are plotted as a function of time. The top and bottom boundaries were measured by tracking the positions of the filter discs. The other boundaries were averaged from the positions of the grid points, which were measured with the block-matching algorithm.

became lower than some predetermined threshold value. Here, the minimum value of the MSD was used as a measure of the degree of correlation between the blocks. For perfect correlation the value is zero and for fully uncorrelated blocks ( $\langle B \cdot B_{\text{ref}} \rangle = \langle B \rangle \cdot \langle B_{\text{ref}} \rangle$ ) the expected value is given by

$$\langle \text{MSD} \rangle_0 = \left\langle (B - B_{\text{ref}})^2 \right\rangle_0 = \langle B^2 \rangle - 2\langle B \rangle \cdot \langle B_{\text{ref}} \rangle + \langle B_{\text{ref}}^2 \rangle \quad (8)$$

The reference block was updated whenever the criterion

$$\min(\text{MSD}) > k \cdot \langle \text{MSD} \rangle_0 \quad (9)$$

was met. An optimal value for the parameter  $k$  was found by calculating the root-mean-square error of the partial densities of bentonite and water between the final result given by the method and the gravimetric validation data as a function of  $k$  (Fig. 5). The two curves, based on both bentonite and water data, have the minima at around  $k=0.15$ , which was thereby chosen to be the low correlation threshold in the

deformation measurement. Fig. 6 shows a set of MSD curves of an arbitrary grid point and illustrates how the calculation of the displacement took place at this particular point.

The block-matching algorithm was applied to the normalized images by forming 50 equally spaced grid points along the axial direction of the sample in the initial state. Reference blocks of size 315 (H)  $\times$  41 (V) pixels, covering the whole width of the sample, were formed around each grid point and the matching blocks were searched from the subsequent images as described above. To improve the signal-to-noise ratio in further analysis, the samples were divided into 10 equally spaced layers in the initial state. The position of the layer boundaries was determined by performing local quadratic fitting to the deformation data. The deformation measurement at the top end of the sample turned out to be difficult as the tracer particles became sparse in that region. Therefore, the displacement of the top end was measured more accurately by tracking the movement of the filter disc. This was done by fitting a sigmoid-type function to the axially averaged profiles of the linear attenuation coefficient in the vicinity of the upper end of the sample. Similar fit was also used for the bottom end, although the displacement there was minimal. Fig. 7 shows an example of the measured deformation, where the positions of the grid points and the layer boundaries are plotted as a function of time. Similar deformation plots for all the samples can be found in section C in the supplementary material.

The deformation analysis is based on the assumption that the tracer particles strictly follow the motion of bentonite in all parts of the sample, including especially the upper part where the water content became high. The validity of this assumption was confirmed by a separate sedimentation test discussed in section B in the supplementary material.

#### 4.4. Relative attenuation coefficient

By assuming the linear attenuation coefficient of the tube wall ( $\mu_t$ ) and the sample ( $\mu_s$ ) to be constants along the beam direction (see Eq. 1), the aluminum equivalent thickness is given by

$$s_r = \mu'_t \cdot s_t + \mu'_s \cdot s_s, \quad (10)$$

where  $\mu'_t = \mu_t / \mu_r$  and  $\mu'_s = \mu_s / \mu_r$  are the relative attenuation coefficients ( $\mu_r$  is the linear attenuation coefficient of the reference material), and  $s_t$  and  $s_s$  are the beam travel distances inside the tube wall and the sample, respectively. The travel distances were calculated by assuming the parallel beam geometry (Fig. A.1, supplementary material). This

assumption is justified as the source-to-sample distance (243 mm) was much larger than the tube diameter (12 mm). The relative attenuation coefficient of the tube was calculated individually for each sample from the empty tube area in the initial state image by setting  $\mu_s' = 0$  in Eq. 10 and then averaging the obtained 2D relative attenuation coefficient image into a single value using the weighted average

$$\bar{\mu}_t' = \frac{\sum_i \sum_j (s_{t,ij} \cdot \mu'_{t,ij})}{\sum_i \sum_j s_{t,ij}}, \quad (11)$$

where  $i$  and  $j$  are the indices of image pixel rows and columns, respectively. The mean and standard deviation of the relative attenuation coefficient for the 16 aluminum sample holder tubes were found to be  $0.980 \pm 0.014$ . The relative attenuation coefficient of the sample was calculated for each pixel using Eq. 10 with  $\mu_t' = \bar{\mu}_t'$ . The resulting 2D relative attenuation coefficient image was further averaged row by row to produce an axial distribution of the relative attenuation coefficient of the sample material as the weighted average

$$\mu'_{s,i} = \frac{\sum_j (b_{ij} \cdot s_{s,ij} \cdot \mu'_{s,ij})}{\sum_j (b_{ij} \cdot s_{s,ij})}, \quad (12)$$

where  $b_{ij}$  is the pixel value of the binary mask image at row  $i$  and column  $j$  (see section 4.2). The binary mask image is used here to exclude the tracer particles from the calculation.

#### 4.5. Density calibration

By using the mixture rule (Eq. 2), the relative attenuation coefficient of the sample, consisting of bentonite and water, can be written as

$$\mu'_s = c'_b \cdot \rho_b + c'_w \cdot \rho_w, \quad (13)$$

where  $c_b' = c_b/\mu_r$  and  $c_w' = c_w/\mu_r$ . The attenuation of air, present in the sample, was neglected due to its low density and low attenuation. The coefficients  $c_b'$  and  $c_w'$  were calculated by performing a two-point calibration individually for each sample. By using the initial state of the sample and the water layer in the subsequent images, the coefficients were solved from the equations

$$c'_b \cdot \bar{\rho}_{b0} + c'_w \cdot \bar{w}_0 \cdot \bar{\rho}_{b0} = \bar{\mu}'_{s0}, \quad (14)$$

$$c'_b \cdot 0 + c'_w \cdot \bar{\rho}_{wl} = \bar{\mu}'_{wl}, \quad (15)$$

where  $\bar{\rho}_{b0}$ ,  $\bar{w}_0$  and  $\bar{\mu}'_{s0}$  are the average dry density, water content and relative attenuation coefficient of the sample in the initial state, and  $\bar{\rho}_{wl} = 1.00 \text{ g/cm}^3$  and  $\bar{\mu}'_{wl}$  are the average density and relative attenuation coefficient of the water layer, respectively. The mean and standard deviation of the coefficients  $c_b'$  and  $c_w'$  for the 16 samples were found to be  $(0.3814 \pm 0.0065) \text{ cm}^3/\text{g}$  and  $(0.1709 \pm 0.0059) \text{ cm}^3/\text{g}$ , respectively.

#### 4.6. Partial density of bentonite and water

During the swelling process, the mass of bentonite is conserved within each vertical layer of the sample as the layer boundaries follow the motion of bentonite. Applying Eq. 13 on a given layer in the initial state yields the mass of bentonite in the layer as

$$m_b = \frac{\mu'_{s0} \cdot V_0}{c'_b + w_0 \cdot c'_w}, \quad (16)$$

where  $\mu'_{s0}$  and  $V_0$  are the relative attenuation coefficient and volume of the layer in the initial state, respectively. The partial density of bentonite in the same layer in a deformed state is thus given by

**Table 4**

Measured dry density ( $\rho_{b0}$ ), water content ( $w_0$ ), degree of saturation ( $S_0$ ) and density gradient ( $d\rho_{b0}/dz$ ) of samples in the initial state, and top end displacement ( $u_t$ ) and occurrence of clearly visible voids in the final state. The dry density was calculated using accurate sample dimensions from X-ray images. The degree of saturation was calculated as  $S_0 = w_0 \cdot \rho_{b0}/\rho_{w,\text{sat}}$  where  $\rho_{w,\text{sat}}$  is the partial density of water at saturation (Eq. 19). The density gradient was determined by performing a linear fit to the initial density profile.

Sample name	Original name	$\rho_{b0}$ [g/cm <sup>3</sup> ]	$w_0$ [%]	$S_0$ [%]	$d\rho_{b0}/dz$ [g/cm <sup>4</sup> ]	$u_t$ [cm]	Visible voids
1A	FS20	1.40	12.0	34.1	0.110	2.21	Yes
1B	FS27	1.42	11.9	34.9	0.095	1.39	Yes
2A	FS23	1.37	17.1	46.8	0.079	1.12	Yes
2B	FS28	1.42	17.8	52.2	0.108	1.81	Yes
3A	FS25	1.45	23.9	72.8	0.107	0.66	No
3B	FS30	1.42	24.4	71.2	0.102	0.72	No
4A	FS17	1.66	12.1	50.3	0.146	1.43	Yes
4B	FS22	1.62	12.0	47.5	0.109	1.00	No
5A	FS16	1.62	17.4	68.3	0.124	1.26	Yes
5B	FS18	1.62	16.6	65.4	0.123	1.18	No
6A	FS14	1.62	24.1	94.9	-0.013	0.92	Yes
6B	FS19	1.63	24.0	96.4	0.014	0.72	Yes
7A	FS26	1.86	12.0	68.5	0.119	0.93	No
7B	FS31	1.87	11.9	69.4	0.130	1.36	Yes
8A	FS24	1.84	17.1	94.4	0.063	0.68	No
8B	FS29	1.76	17.8	86.5	0.036	1.20	Yes

$$\rho_b = \frac{m_b}{V} = \frac{\mu'_{s0} \cdot V_0 / V}{c'_b + w_0 \cdot c'_w}, \quad (17)$$

where the volume ratio of the layer  $V_0/V$  is readily obtained based on the measured deformation. Finally, the partial density of water in the layer is given by Eq. 13 as

$$\rho_w = \frac{\mu'_s - c'_b \cdot \rho_b}{c'_w}. \quad (18)$$

## 5. Results

The complete set of results of the 16 individual experiments carried out are available at DOI: <https://doi.org/10.5281/zenodo.5413932> (Harjupatana et al., 2021).

### 5.1. Initial values and density gradients

**Table 4** shows the measured dry density, water content, degree of saturation and density gradient in the initial state for all the samples. Also is given the measured displacement of the top end and the occurrence of clear voids in the final state (discussed later). The measured initial dry densities of the samples deviated slightly from the target values ( $1.40 \text{ g/cm}^3$ ,  $1.65 \text{ g/cm}^3$  and  $1.80 \text{ g/cm}^3$ ), because the target height of the samples (2 cm) was difficult to achieve accurately. The samples slightly expanded right after the compaction, which was difficult to predict and compensate either by slightly overcompacting or by increasing the target mass of the sample. Most of the samples had an average initial density gradient of around  $0.1 \text{ g/cm}^4$ , and thus the top end was around  $0.2 \text{ g/cm}^3$  denser than the bottom end. The initial density gradients were caused by wall friction during the sample compaction (Michrafy et al., 2003). In uniaxial powder compaction, with a die and a single-acting punch on the top, the wall shear stress between the powder and the die opposes the motion of the powder. As a result, the magnitude of total friction force increases downward due to increasing wall area. This causes the compressive stress and hence the density to decrease downward. This common issue in powder compaction cannot be completely eliminated, but may be reduced by using a lower aspect ratio ( $h/d$ ) of the sample and lubrication (Tien et al., 2007). However, samples 6A, 6B, 8A and 8B showed much smaller density

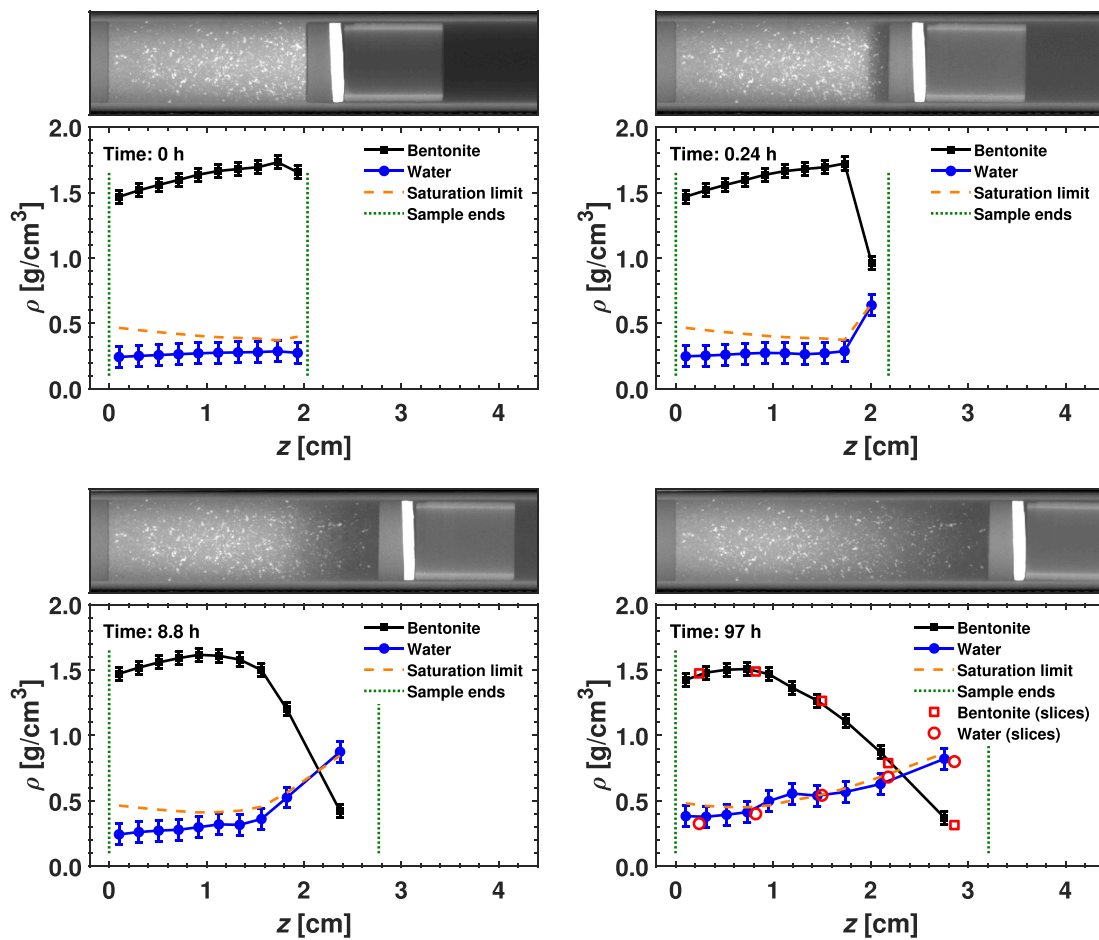


**Fig. 8.** Example of main results for sample 5B ( $\rho_{b0} \approx 1.65 \text{ g/cm}^3$ ,  $w_0 \approx 17\%$ ). The measured partial density profiles of bentonite and water, the saturation limit, and the corresponding aluminum equivalent thickness images are shown at four instants of time. Also shown are the validation data in the last subfigure.

gradients. Those samples were compacted near the saturation limit ( $S_0=100\%$ ), at which the sample material becomes nearly incompressible. This forces the density profile to be flat provided that no redistribution of water occurs.

## 5.2. Partial densities of bentonite and water

Here, only a few examples of the main results are shown to assess the feasibility of the method and to demonstrate the main qualitative features of the results. Figs. 8 and 9 show examples of the main results, i.e., the axial distributions of partial density of bentonite and water at four instants of time for samples 5B and 6A. These samples had the same initial dry density  $\rho_{b0} \approx 1.65 \text{ g/cm}^3$ , but different initial water content values  $w_0 \approx 17\%$  and  $w_0 \approx 24\%$ , respectively. The corresponding aluminum equivalent thickness images are shown on top of the graphs (rotated to horizontal position). The last subfigures show the final state of the samples together with the gravimetric validation data. The error bars represent the root-mean-square error of the data points ( $\pm 0.05 \text{ g/cm}^3$  for bentonite and  $\pm 0.08 \text{ g/cm}^3$  for water, see Fig. 5). Also shown in the figures is the saturation limit estimated using the formula

$$\rho_{w,\text{sat}} = \rho_w^* \left( 1 - \frac{\rho_b}{\rho_b^*} \right), \quad (19)$$

where  $\rho_w^*$  and  $\rho_b^*$  are the material density of water and bentonite, respectively. Here, the value  $\rho_w^* = 1.00 \text{ g/cm}^3$ , and the commonly used ‘grain density’ value of bentonite  $\rho_b^* = 2.75 \text{ g/cm}^3$  (Table 2) were used. Similar examples of main results for all the samples can be found in

section D in the supplementary material.

While samples 5B and 6A differed only by their initial water content, a few qualitative differences can be observed. Firstly, as was already shown in Table 4 and discussed above about wall friction, sample 5B (Fig. 8) had a marked density gradient in the initial state, whereas sample 6A (Fig. 9) had a very flat initial density profile. Another difference between the two samples can be seen in the late stage of swelling behavior in the top part of the samples. While sample 5B (Fig. 8) remained locally rather homogeneous throughout the experiment, clear inhomogeneities occurred in the final state of sample 6A (Fig. 9). Comparing the measured water content curve and the validation data with the saturation limit shows that the top end of sample 6A was unsaturated in the final state. This indicates that the observed inhomogeneities were likely voids created by gas accumulation. The gas may have originated from compressed pore air trapped during the compaction and from residual air dissolved in the water. Such visible inhomogeneities were observed in the most dilute upper parts of some of the samples in the final state (Table 4). However, the appearance of the voids does not seem to correlate with the initial dry density and water content values. In general, the overall swelling behavior was qualitatively similar and systematic between all the samples. The wetting and swelling were very fast in the beginning, but slowed down considerably over time (see deformation plots in Fig. 7 and in section C in the supplementary material). The bentonite in the upper part became fully saturated, which effectively suppressed water transport deeper into the sample due to low permeability in the saturated zone. In the final state, the upper part of the sample was saturated (apart from the gas filled

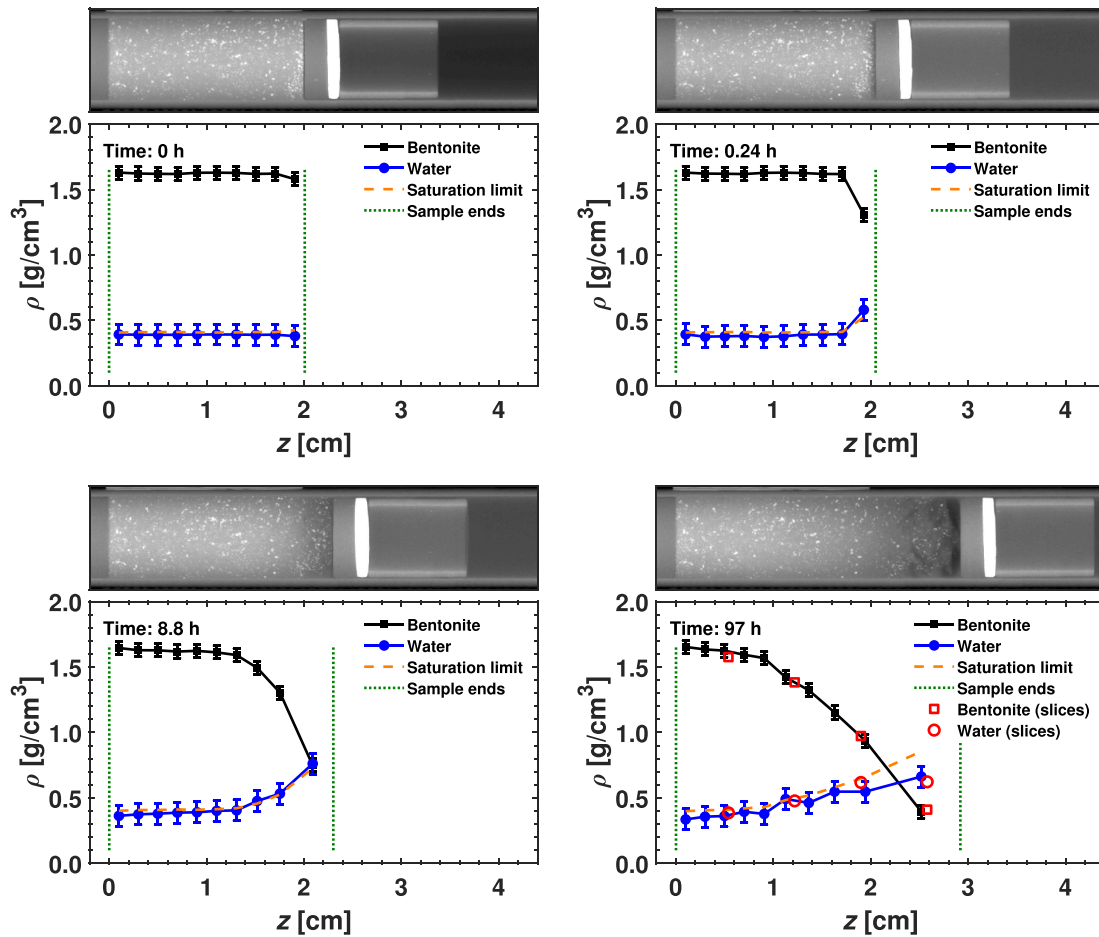


**Fig. 9.** Example of main results for sample 6A ( $\rho_{b0} \approx 1.65 \text{ g/cm}^3$ ,  $w_0 \approx 24\%$ ). The measured partial density profiles of bentonite and water, the saturation limit, and the corresponding aluminum equivalent thickness images are shown at four instants of time. Also shown are the validation data in the last subfigure.

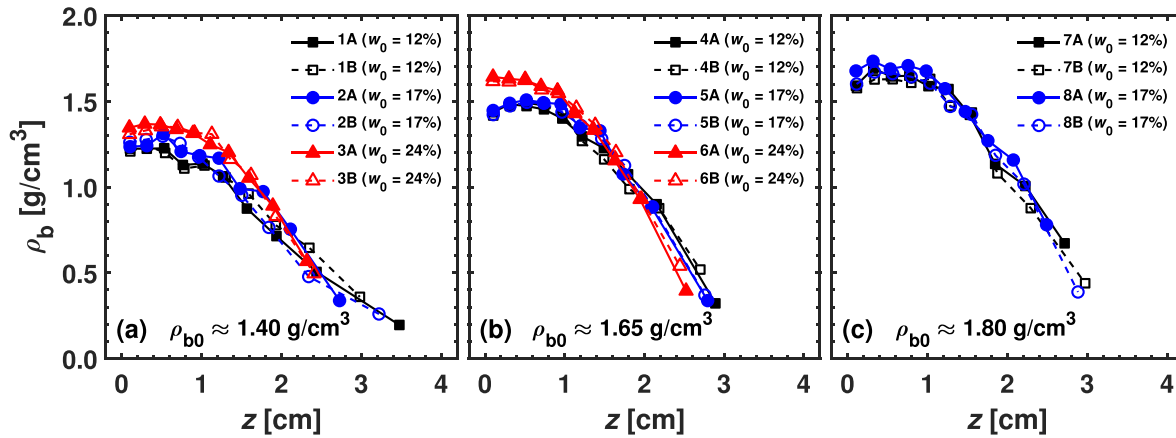


**Fig. 10.** Dry density profiles for low (a), middle (b) and high (c) density samples in final state.

voids), while the lower part remained unsaturated (if not initially saturated). Obviously, the duration of the experiments covered only the initial stage of the swelling process to maximum dilution, and hence no stationary state was reached during four days of wetting. The local deformation of material was large and initially rapid, and despite the optimized deformation analysis, small errors in the measured displacements occurred. These errors were caused, e.g., by deviations from the one-dimensional swelling behavior, by non-uniform distribution of

tracer particles, by low concentration of tracer particles in the most swollen regions and by occasional spurious behavior of tracer particles near the tube wall and at the seams of the stitched images. These errors led to increasing scatter of the partial density profiles of bentonite and water. Ideally, the errors in the partial densities are related as  $\Delta\rho_w = -c'_w/c_w \cdot \Delta\rho_b \approx -2.2 \cdot \Delta\rho_b$  (derived from Eq. 13, assuming  $\Delta\mu_s' = 0$ ). This explains why the partial density profiles of water are generally more noisy than those of bentonite, and why the erroneous data points seem to

**Table 5**

Details and results of some one-dimensional bentonite swelling experiments from literature. Columns:  $\rho_{b0}$  = initial dry density,  $w_0$  = initial water content,  $d$  = sample diameter,  $h_0$  = initial sample height, PD = porous disc on top (Yes/No),  $c(\text{Na}^+)$  = sodium concentration in water,  $c(\text{Ca}^{2+})$  = calcium concentration in water,  $u_t$  = top end displacement after 4 days of swelling (approximated from graphs). Notes: CB = Commercial Na-bentonite.

Bentonite	$\rho_{b0}$ [g/cm <sup>3</sup> ]	$w_0$ [%]	$d$ [cm]	$h_0$ [cm]	PD	$c(\text{Na}^+)$ [M]	$c(\text{Ca}^{2+})$ [M]	$u_t$ [cm]	Reference
MX-80	1.74	17	5.0	4.0	Yes	0.000	0.000	1.5	Sane et al. (2013)
MX-80	1.74	17	5.0	4.0	Yes	0.111	0.032	2.0	Sane et al. (2013)
MX-80	1.75	17	5.0	4.0	No?	0.000	0.000	2.7	Navarro et al. (2017)
MX-80	1.75	17	5.0	4.0	No?	0.111	0.032	2.8	Navarro et al. (2017)
CB	1.20	30	3.7	1.0	No	0.000	0.000	1.8	Li et al. (2019)
CB	1.20	30	3.7	1.0	No	0.100	0.000	1.6	Li et al. (2019)

be in the opposite directions (minus sign). Nevertheless, the results obtained agree reasonably well with the validation data.

### 5.3. Final state dry density profiles and total swelling

Fig. 10 shows the measured dry density profiles in the final state for all the samples. The general shape of the curves is similar despite the different initial dry density and water content values. The dry density profiles between the repeated experiments (A vs B) are very similar but differ near the top of the samples, where the largest contribution to the total swelling comes. The top end displacements ( $u_t$ ) indeed show large variations both between different cases and between repeated experiments (Table 4). It seems that the samples with visible voids swelled more than those remaining locally homogeneous. Due to the scattered values, it is difficult to see correlation between the initial values and the top end displacements.

Similar one-dimensional bentonite swelling experiments have been performed, e.g., by Sane et al. (2013), Navarro et al. (2017) and Li et al. (2019). In those studies, the total swelling of compacted bentonite samples was visually monitored through transparent sample tubes. Table 5 shows details and results of some relevant experiments of their studies to compare here. In general, the top end displacements in their experiments were somewhat greater than here. This was probably due to smaller effect of wall friction as the sample diameter was larger and the samples were not directly compacted into the tubes (smaller initial normal stress against tube wall) in their experiments. The total swelling may also depend on the mass of a porous disc placed on the top of the sample as the balancing axial swelling stress of the dilute top part may be very small and sensitive to small changes. Sane et al. (2013) used porous stainless steel discs, whereas Li et al. (2019), and possibly also Navarro et al. (2017), did not use discs.

## 6. Conclusions

A method based on X-ray imaging for monitoring one-dimensional wetting and swelling of bentonite in a narrow tube was introduced. The method yields the deformation and the partial density distributions of bentonite and water as a function of time. The deformation of the samples was measured using tracer particles and a specific image correlation technique. The measurement of the partial densities of bentonite and water was based on careful calibration utilizing the measured effective X-ray attenuation coefficient. The developed local beam hardening correction was found to be essential for quantitative density analysis based on X-ray images.

An obvious technical drawback of the method is the limited accuracy of the displacement analysis, at least as applied in the present case where rapid and large deformations occurred. Furthermore, the measured partial densities of bentonite and water appeared to be quite sensitive to errors made in displacement analysis which in some cases led to marked scatter in the measured density profiles. In spite of that, the results obtained here are consistent and agree, in general, relatively well with the validation data obtained gravimetrically from the samples in the final state of the experiment.

Most of the samples showed an initial density gradient caused by

wall friction during sample compaction. The effect of wall friction during the compaction was pronounced here due to the high aspect ratio of the samples ( $h/d = 2$ ). Wall friction was also likely present in the experiments and restricted the swelling process to some extend. In some of the experiments spurious inhomogeneities, most likely caused by accumulation of air to form voids, were observed especially in the upper parts of the sample at late stage of the experiment. Although such phenomena do not compromise the applicability of the present experimental method as such, they may hamper the use and interpretation of the data, e.g., in model validation purposes. Due to wall friction and void formation, the results may reflect more real conditions, swelling and wetting of bentonite in a narrow fracture, than ideal free swelling conditions. To fully utilize the results obtained, one may need a more sophisticated material model that takes into account these non-idealities.

The method proved to be useful for monitoring wetting and swelling of bentonite in the experimental setup in this study. It yielded potentially valuable data on hydro-mechanical properties of bentonite, which can be used to develop and validate material and transport models regarding the behavior of bentonite buffer. Compared to traditional methods, where total swelling is only measured, the X-ray imaging method can be used to produce much more detailed data on wetting and swelling behavior of bentonite to support modeling even better.

Finally, the method introduced here might be even more applicable in cases with more moderate rate and degree of deformation, such as wetting and swelling of bentonite in a confined volume. The method developed here is not restricted only to the materials used in this study, but may be applied for non-destructive monitoring of simultaneous liquid transport and related deformation with a variety of materials that allow X-ray imaging and contain natural or artificially added heterogeneities which are visible in X-ray images and can be used to measure the deformation. Furthermore, the local beam hardening correction can be applied more generally to facilitate more accurate image analysis and image-based measuring techniques in X-ray imaging and tomography.

## CRediT authorship contribution statement

**Tero Harjupatana:** Methodology, Software, Formal analysis, Investigation, Writing – original draft, Visualization. **Artru Miettinen:** Writing – review & editing. **Markku Kataja:** Conceptualization, Methodology, Software, Formal analysis, Writing – review & editing, Supervision, Project administration, Funding acquisition.

## Declaration of Competing Interest

The authors declare that they have no known competing financial interests or personal relationships that could have appeared to influence the work reported in this paper.

## Acknowledgments

The research leading to these results has received funding from the European Atomic Energy Community's 7th Framework Programme (FP7/2007-2011) under grant agreement no. 295487.

## Appendix A. Supplementary data

Supplementary data to this article can be found online at <https://doi.org/10.1016/j.clay.2022.106485>.

## References

- Börjesson, L., Gunnarsson, D., Johannesson, L.-E., Jonsson, E., 2010. Design, Production and Initial State of the Buffer. Technical Report. SKB.
- Bushberg, J.T., Seibert, J.A., Leidholdt, E.M., Boone, J.M., 2002. The Essential Physics of Medical Imaging, 2 edition. Lippincott Williams & Wilkins.
- Gustschin, N., Gustschin, A., Epple, F., Allner, S., Achterhold, K., Herzen, J., Pfeiffer, F., 2019. Signal-to-thickness calibration and pixel-wise interpolation for beam-hardening artefact reduction in microCT. *EPL (Europhysics Letters)* 125 (3), 38003.
- Harjupatana, T., Alaraudanjoki, J., Kataja, M., 2015. X-ray tomographic method for measuring three-dimensional deformation and water content distribution in swelling clays. *Appl. Clay Sci.* 114, 386–394.
- Harjupatana, T., Miettinen, A., Kataja, M., 2021. Swelling of MX-80 bentonite in a narrow tube. *Zenodo 2021*. <https://doi.org/10.5281/zenodo.5413932>.
- Hellä, P., Pitkänen, P., Löfman, J., Partamies, S., Vuorinen, U., Wersin, P., 2014. Safety Case for the Disposal of Spent Nuclear Fuel at Olkiluoto: Definition of Reference and Bounding Groundwaters, Buffer and Backfill Porewaters. Posiva. <https://cris.vtt.fi/en/publications/safety-case-for-the-disposal-of-spent-nuclear-fuel-at-olkiluoto-d>.
- Herman, G.T., 1979. Correction for Beam Hardening in Computed Tomography. *Phys. Med. Biol.* 24 (1), 81–106.
- Hsieh, J., Molthen, R.C., Dawson, C.A., Johnson, R.H., 2000. An iterative approach to the beam hardening correction in cone beam CT. *Med. Phys.* 27 (1), 23–29.
- Hubbell, J.H., Seltzer, S.M., 1995. Tables of X-Ray Mass Attenuation Coefficients and Mass Energy-Absorption Coefficients 1 keV to 20 MeV for Elements Z = 1 to 92 and 48 Additional Substances of Dosimetric Interest. Technical Report. National Institute of Standards and Technology.
- Johns, H.E., Cunningham, J.R., 1983. The Physics of Radiology, 4 edition. Charles C. Thomas.
- Jung, S.Y., Lim, S., Lee, S.J., 2012. Investigation of water seepage through porous media using X-ray imaging technique. *J. Hydrol.* 452, 83–89.
- Juvankoski, M., 2013. Buffer Design 2012. Technical Report, Posiva Oy.
- Karnland, O., 2010. Chemical and Mineralogical Characterization of the Bentonite Buffer for the Acceptance Control Procedure in a KBS-3 Repository. Technical Report. Swedish Nuclear Fuel and Waste Management Co.
- Karnland, O., Olsson, S., Nilsson, U., 2006. Mineralogy and Sealing Properties of Various Bentonites and Smectite-Rich Clay Materials. Technical Report. Swedish Nuclear Fuel and Waste Management Co.
- Koch, D., 2002. Bentonites as a basic material for technical base liners and site encapsulation cut-off walls. *Appl. Clay Sci.* 21 (1–2), 1–11.
- Li, X., Xu, Y., Li, C., 2019. Experimental study on the 1-d free swelling of compacted bentonite. *Acta Geotech.* 1–13.
- Michrafy, A., Kadiri, M.S., Dodds, J.A., 2003. Wall friction and its effects on the density distribution in the compaction of pharmaceutical excipients. *Chem. Eng. Res. Des.* 81 (8), 946–952.
- Miettinen, A., Harjupatana, T., Kataja, M., Fortino, S., Immonen, K., 2016. Time-Resolved X-Ray Microtomographic Measurement of Water Transport in Wood-Fibre Reinforced Composite Material. In: IOP Conference Series: Materials Science and Engineering, vol. 139. IOP Publishing, p. 012037.
- Nagra, 2009. The Nagra Research, Development and Demonstration (RD&D) Plan for the Disposal of Radioactive Waste in Switzerland.
- Navarro, V., Yustres, Á., Asensio, L., De la Morena, G., González-Arteaga, J., Laurila, T., Pintado, X., 2017. Modelling of compacted bentonite swelling accounting for salinity effects. *Eng. Geol.* 223, 48–58.
- Neretnieks, I., Liu, L., Moreno, L., 2009. Mechanisms and Models for Bentonite erosion.
- Reid, C., Lunn, R., El Mountassir, G., Tarantino, A., 2015. A mechanism for bentonite buffer erosion in a fracture with a naturally varying aperture. *Mineral. Mag.* 79 (6), 1485–1494.
- Sane, P., Laurila, T., Olin, M., Koskinen, K., 2013. Current Status of Mechanical erosion Studies of Bentonite Buffer. Technical Report, Posiva Oy.
- Shafizadeh, A., Gimmi, T., Van Loon, L., Kaestner, A., Lehmann, E., Maeder, U.K., Churakov, S.V., 2015. Quantification of water content across a cement-clay interface using high resolution neutron radiography. *Phys. Procedia* 69, 516–523.
- Terskikh, V.V., Feurtado, J.A., Ren, C., Abrams, S.R., Kermode, A.R., 2005. Water uptake and oil distribution during imbibition of seeds of western white pine (*Pinus monticola* Dougl. Ex D. Don) monitored *in vivo* using magnetic resonance imaging. *Planta* 221 (1), 17–27.
- Tien, Y.-M., Wu, P.-L., Huang, W.-H., Kuo, M.-F., Chu, C.-A., 2007. Wall friction measurement and compaction characteristics of bentonite powders. *Powder Technol.* 173 (2), 140–151.
- Zhou, X., Zhou, J., Kinzelbach, W., Stauffer, F., 2014. Simultaneous measurement of unfrozen water content and ice content in frozen soil using gamma ray attenuation and TDR. *Water Resour. Res.* 50 (12), 9630–9655.
- Zhou, R., Zhou, X., Li, X., Cai, Y., Liu, F., 2016. Study of the Microfocus X-ray Tube based on a Point-like Target used for Micro-Computed tomography. *PLoS One* 11 (6), e0156224.
- Zou, W., Hunter, N., Swain, M.V., 2011. Application of Polychromatic CT for Mineral Density Determination. *J. Dent. Res.* 90 (1), 18–30.